MSOT-guided nanotheranostics for synergistic mild photothermal therapy and chemotherapy to boost necroptosis/apoptosis

Shiying Li[a‡], Kwok-Ho Lui[a‡], Wing-Sum Lau[b], Juyu Chen[b], Wai-Sum Lo[a], Xin Li[a], Yan-Juan Gu[*a], Liang-ting Lin[*b], Wing-Tak Wong[*a,c]

a Department of Applied Biology and Chemical Technology, The Hong Kong Polytechnic University, Hung Hom, Hong Kong, China.
b Department of Health Technology and Informatics, The Hong Kong Polytechnic University, Hung Hom, Hong Kong, China.
c The Hong Kong Polytechnic University Shenzhen Research Institute, Shenzhen 518057, China

ABSTRACT: The development of nanotheranostics for precision imaging-guided regulated cell death (RCD)-mediated synergistic tumor therapy is still challenging. Herein, a novel multifunctional nanotheranostic agent, iRGD-coated maleimide-poly(ethylene glycol)-poly(lactic acid/glycolic acid) (iRGD-Mal-PEG-PLGA) encapsulated hydrophobic gold nanocages (AuNCs) and hydrophilic epigallocatechin gallate (EGCG) (PAuE) is developed for multispectral optoacoustic tomography (MSOT)-guided photothermal therapy (PTT) and chemotherapy. The portion of necroptotic and apoptotic tumor cells were 52.9 % and 5.4 % at 6 hrs post-incubation after AuNC-induced mild PTT treatment, whereas they became 14.0 % and 46.1 % after 24 hrs, suggesting that the switch of cell death pathway is a time-dependent process. Mild PTT facilitated the release of EGCG which induces the downregulation of hypoxia-inducible factor-1 (HIF-1α) expression to enhance apoptosis at a later stage, realizing a remarkable tumor growth inhibition in vivo. Moreover, RNA sequence analyses provided insights about the significant changes in genes related to the crosstalk between necroptosis and apoptosis pathways via PAuE upon laser irradiation. In addition, the biodistribution and metabolic pathways of PAuE have been successfully revealed by 3D MSOT. Taken together, this strategy of first combination of EGCG and AuNCs-based photothermal agent (PTA) via triggering necroptosis/apoptosis to downregulate HIF-1α expression in tumor environment provides a new insight in anticancer therapy.

Corresponding author:

E-mail: Yanjuan.gu@polyu.edu.hk; lt.lin@polyu.edu.hk; w.t.wong@polyu.edu.hk.

1. INTRODUCTION

PTT is a non-invasive and localized tumor treatment modality that holds promise and has attracted extensive research attention in recent years due to its high selectivity and limited adverse side effects.[1,2] In order to ablate tumors completely, a high-energy throughput photothermal heating (temperature over 50 °C) is required to induce necrosis in tumors.[3,4] Nevertheless, inevitable damage to surrounding healthy regions is derived from non-localized heat and hyperthermia.[5,6] Moreover, cancer cells absorb heat and generate thermoresistance, with a significantly increased expression of heat shock proteins (Hsps) attributing to apoptosis resistance and decreased cytotoxicity.[7–9] In addition, overheating the tumor tissue in PTT treatment would induce high levels of hypoxia-inducible factor-1 (HIF-1α) in the tumor hypoxia region, which reduces the therapeutic efficacy of chemo-drugs.[10] Therefore, mild hyperthermia *via* PTT (42-49 °C) is preferred for clinical applications. It has also been proven that cancer cell membranes at a mild hyperthermia temperature range exhibit enhanced permeability and fluidity which aids the intracellular uptake of chemo-drugs.[11,12] Mild PTT is often been used in conjunction with traditional chemotherapy,[13–16] molecularly targeted drugs,[17,18] gene therapy[19] and immunotherapy[20,21] to maximize anticancer effects. Researchers have revealed that PTT combined with chemotherapy offers several advantages compared to individual therapies: it is one of the non-invasive therapies with high efficiency in eliminating cancer cells at low temperatures, the adjustable dosage of PTAs can be precisely located at tumor region, minimize dosage of chemo-drug, the minimize the damage to the healthy cells.[22]

Apoptosis and necrosis were long thought to be the main regulated cell death (RCD) pathways. Recent studies demonstrated that triggering necroptosis to orchestrate cell death is an effective therapeutic strategy to overcome apoptosis resistance in cancer.[23] Necroptosis is known as a novel caspase-independent RCD modality that highlights the importance of changes of necrosis-like morphology, as well as mediating receptor-interacting protein (RIP) kinase-like RIP1 and RIP3, and mixed lineage kinase domain-like (MLKL) proteins.[24,25] In the past decade, cell death mechanisms such as apoptosis, necroptosis and pyroptosis have been considered to employ parallel pathways to kill cells. Currently, increasing evidence discloses that apoptosis and necroptosis are tightly connected to coordinate cell death.[26,27] Previous studies have shown that different nanomaterials-mediated PTT such as carbon dots, black phosphorus, CuS-NiS, and gold nanostructurs will trigger necroptosis to induce tumor cell death.[28–32] Nevertheless, the occurrence of necroptosis pathways *via* nanomaterials and the role of necroptosis in PTT/chemotherapy are still topics of controversy and warrants more investigation. Hence, we proposed to develop a novel "all in one" nanoplatform, comprehensively contributing to the "programmed cell death" *via* both necroptotic and apoptotic mechanisms, which might demonstrate the key function of mild PTT. Epigallocatechin gallate (EGCG), the main component in green tea, is a novel class of powerful anti-oxidant that interrupts the generation and metastasis of different cancers types such as brain, liver and breast cancers.[33,34] More and more studies proved that the EGCG anti-cancer mechanism is related to suppressing early angiogenesis, cancer cell death induction and inhibition of cancer cells metastasis.[35–39] Nevertheless, the biomedical application of EGCG *in vivo* is restricted by insufficient stability, low bioavailability and fast clearance rate in living objects.[40] Therefore, several EGCG-nanovehicles have been designed to improve the stability, bioavailability and improve the efficacy of cancer treatment.[41] In addition, to significantly improve the therapeutic effects in EGCG-involved nanovehicles, it is necessary to integrate EGCG and other drug molecules with different functions in a single nanostructured entity. The combination of EGCG with other chemical drugs, gene therapy, and photodynamic therapy (PDT) has been reported.[42–44] Despite recent endeavors to utilize DOX-loaded EGCG-Fe(III) to realize PTT and chemotherapy simultaneously, the combination between EGCG and PTA is still rare.[45]

Anisotropic gold nanostructures have unique advantages in photothermal properties and nanocarriers to deliver drug molecules, but their biomedical application in EGCG loading for combined PTT and chemotherapy is rarely exploited.[46] To date, AuNCs hold great promises as novel MSOT imaging contrast agents and drug carriers because they enable the conversion of light into heat effectively and own hollow interior structure with high drug loading efficacy.[13,47–50] Nevertheless, the intrinsic hollow interiors and pores of the AuNCs could lead to premature drug leakage *in vivo*. Hence, it is necessary to prepare a stimuli-responsive coating layer for AuNCs to prevent premature leakage.[51] The hydrophilic block of PEG-PLGA copolymer could increase the systemic circulation time with favorable degradation and multifunctional property, which have attracted much attention for the development of smart drug delivery system.[52,53] To meet the challenges of multidrug resistance of tumor microenvironment, the localized surface plasmon resonance (LSPR) property of AuNCs with high photothermal converting capacity to combined EGCG as chemo-drug *via* emulsion for enhanced synergistic therapy and PAI capability. Besides EGCG can significantly inhibit the expression of VEGF, HIF-1α.[54] This combination in cancer treatment can also block VEGF signal transduction pathways to inhibit tumor angiogenesis and metastasis.[55] In consideration of these advantages of AuNCs and PEG-PLGA, we encapsulated AuNCs and EGCG with PEG-PLGA, followed by conjugation with tumor-targeting peptide iRGD to obtain the final product iRGD-PEG-PLGA@AuNCs/EGCG (denoted as PAuE). The generated nanoplatform was used to

investigate the therapeutic efficacy and the function of mild PTT (Scheme 1). EGCG, on the other hand, performs chemotherapy. In order to investigate the mechanism of mild PTT-mediated cell death pathway, necroptosis and apoptosis are carefully investigated by modulating the incubation time upon laser irradiation, which downregulates the expression of HIF-1α induced by EGCG in the tumor environment. So far this is the first work to combine the chemo-drug EGCG and nanomaterial-based PTA for synergistic cancer therapy. relationship between the necroptosis and apoptosis cell death pathway induced by nanotheranostics.
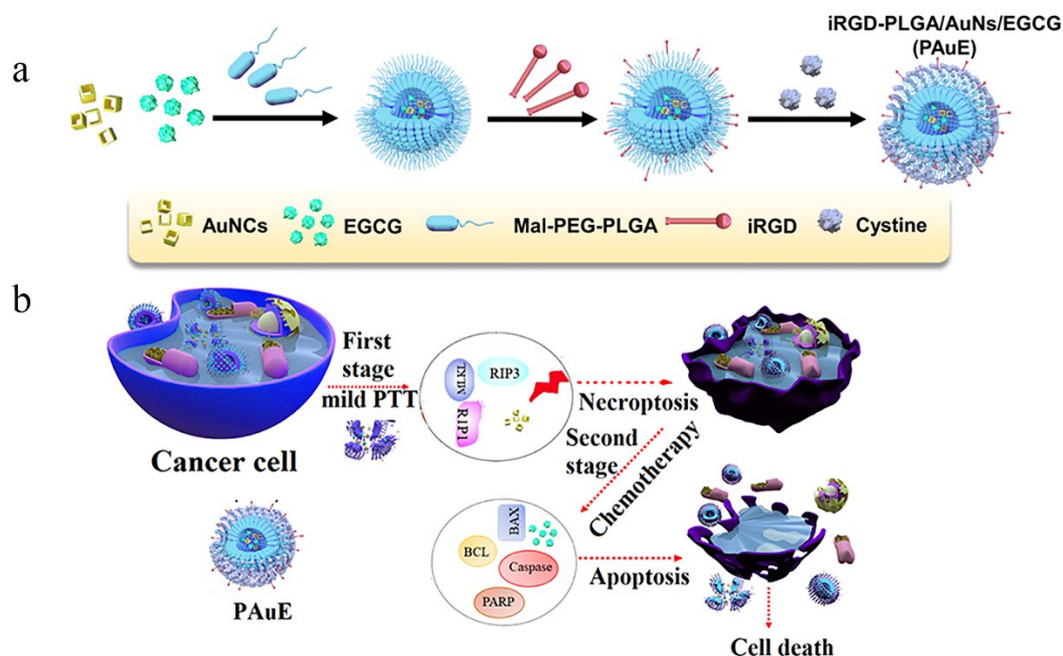
Scheme 1. (a) Schematic of the preparation of PAuE nanoplatform. (b) The necroptosis and apoptosis mechanism induced by PAuE after laser irradiation.

2. Material and methods

2.1 Chemical and reagents. Chloroauric acid hydrate (HAuCl$_4$·4H$_2$O), sodium borohydride (NaBH$_4$), sodium citrate silver nitrate (AgNO$_3$), hydroxylamine hydrochloride (NH$_2$OH·HCl) were purchased Sigma Aldrich. Di-block copolymer maleimide-poly(ethylene glycol)-poly(lactide-co-glycolide)-COOH were purchased from Ruixi Biological Technology (China).

2.2 Cell culture experiment. MDA-MB-231 breast cancer cells (ATCC) were cultured in Dulbecco Modified Eagle Medium (DMEM, Thermo Fisher Scientific Inc.) supplemented with 10 % fetal bovine serum and 100 units/mL penicillin and 100 μg/mL streptomycin with humidified air containing 5 % CO$_2$ in 37 °C. Cells were pre-incubated with 20 μM Nec-1 (MedChemExpress, Princeton, NJ, USA) for 2 hrs followed by the above procedures, which was set as negative control for necroptotic events. Cells were pre-incubated with 20 μM Z-VAD-FMK (In VivoGene) for 2 hrs, serving as a negative control for apoptotic events.

2.3 Animals model. Female Balb/c Nude mice (Balb/C, 5 weeks, female, 20-25 g) acquired from the Animal Center of The Hong Kong Polytechnic University were used for the tumor-bearing model. MDA-MB-231 cells (3 x 10^6) were mixed in matrigel/DMEM (40 μl) solution and injected into the inguinal gland of the mammary fat pad. Studies were initiated until tumors reached 80 mm^3.

2.4 Preparation of iRGD-PEG-PLGA/AuNCs/EGCG (PAuE) NPs. Preparation of gold nanocage (AuNCs) and dodecanethiol-modified AuNCs (Dod@AuNCs) were reported detailed in Supporting Information. The Mal-PEG-PLGA copolymer encapsulated AuNCs and EGCG NPs were synthesized according to the nanoprecipitation method with slight modification.[56] MAL-PEG-PLGA@AuNCs/EGCG NPs were conjugated with iRGD peptide to obtain the targeted nanoplatform iRGD-PEG-PLGA@AuNCs/EGCG (PAuE) NPs was illustrated detailed in Supporting Information. Cystine was used for quenching the unreacted Mal groups on the surface of PAuE NPs.

2.5 Characterization of PAuE, PAu and PE NPs. The UV-vis-NIR absorption spectra of the samples were measured with a spectrophotometer (Agilent 8453). Fourier-transform infrared (FTIR) spectra were measured on a Thermo Scientific Nicolet IS50 IR spectrometer using the KBr pellet technique. The hydrodynamic size, zeta potential and stability of NPs were determined using a dynamic light scattering instrument (DLS, ZetasizerNanoZS90, Malvern Instruments Ltd, UK). The morphologies of AuNCs and PAuE were characterized using a transmission electron microscopy (TEM, JEOL JEM-2010). The

AuNCs content in NPs were performed using inductively coupled plasma mass spectrometry (ICP-MS, Agilent 7500). The EGCG loading capacity and encapsulation efficiency was illustrated detailed in Supporting Information.

2.6   *In vitro* cytotoxicity. The standard CCK-8 assay was used to investigate the cytotoxic effect of PAuE, PAu and PE NPs. The experiment detail was illustrated in Supporting Information. Cells were pre-incubated with 20 mM Nec-1 (MedChemExpress, Princeton, NJ, USA) for 2 hrs followed by the above procedures, which was set as negative control for necroptotic events. The absorbance of the mixture was measured at 450 nm on a Spectra Max ® M3 Microplate Reader to determine the cell viability of NPs. The experiment detail for CLSM images is shown in Supporting Information.

2.7   Annexin V-FITC/PI double staining (flow cytometry). The apoptosis induced relative protein expression level via EGCG or PE NPs was determined by the western blot analysis, the detail as illustration in Supporting Information. For the combined effect of PTT and EGCG, MDA-MB-231 cells were seeded in 6-well plate, subsequently incubated with respective groups, (PBS, laser, PE, PAu + laser and PAuE + laser; 40 ppm of AuNCs; 50 μg/ml of EGCG) for 6 hrs. The medium was replaced by PBS before NIR laser irradiation (808 nm, 1.2 W cm^{-2}, 5 min). Then the cells were further incubated for 6 hrs. The protein concentrations were calibrated and determined *via* standard bicinchoninic acid assay and experiment detail as illustrated in Supporting Information.

2.8   Western blot analysis of apoptosis/necroptosis. The apoptosis induced relative protein expression level via EGCG or PE NPs was determined by the western blot analysis, the detail as illustration in Supporting Information. For the combined effect of PTT and EGCG, MDA-MB-231 cells were seeded in 6-well plate, subsequently incubated with respective groups, (PBS, laser, PE, PAu + laser and PAuE + laser; 40 ppm of AuNCs; 50 μg/ml of EGCG) for 6 hrs. The medium was replaced by PBS before NIR laser irradiation (808 nm, 1.2 W cm^{-2}, 5 min). Then the cells were further incubated for 6 hrs. Total protein from MDA-MB-231 cells was extracted using lysis buffer. The protein concentrations were calibrated and determined *via* standard bicinchoninic acid assay and experiment detail as illustrated in Supporting Information.

2.9   *In vivo* MSOT and monitoring. *In vitro and In vivo* MSOT imaging was carried by an MSOT imaging system (inVision 128, iThera Medical). The mice bearing MDA-MB-231 tumor were anaesthetized and scanned with MSOT after intravenous injection of CAuE or PAuE (30 mg/kg of AuNCs). The following wavelengths were chosen for correspondence with the main characteristic imaging wavelengths in the absorption spectra of PAuE NPs (680, 690, 700,

720, 730, 750, 780, 800, 850 and 900 nm) were selected for data reconstruction under a standard back projection algorithm in the experiments. A total of n = 3 nude mice were conducted independent measurements. For each ROI, approximately 50 frames were evaluated. The images reconstruction is illustrated in Supporting Information.

2.10 *In vivo* tumor inhibition efficacy and animal survival. The tumor-bearing mice bearing MDA-MB-231 tumor were randomly divided into six groups (n = 4) and intravenously injected with PBS, PBS+laser, PAu, PAu+laser, PE +laser, PAuE + laser, PAuE, or PE (5 mg/kg EGCG, 30 mg/kg AuNCs, 200 μL), pending PTT treatments. Tumor regions were irradiated by NIR laser 6 hrs after injection (1.2 Wcm^{-2}, 5 mins x 3 times). Continuous-wave Nd: YAG (LSR808H-2W) laser was used as the light source for mild PTT. The surface temperature was recorded using a thermal camera (FLUKE camera and quantified by the Smart View 4.3 software). Tumor volumes were calculated following a well-established formula. V = (a*b*b)/2 where a and b stand for the longest and shortest diameters of the tumor, respectively. For the overall survival study, 30 tumor-bearing mice were randomly set into six groups (n=5) with respective treatment regimen. After the endpoint, Kaplan-Meier survival curves were plotted for the statistical analysis.

2.11 Immunohistochemistry staining and histopathological evaluation of tumor. Tumor-bearing mice were sacrificed after respective treatments, including PBS, PBS+ laser, PAuE, PAuE + laser, PAu + laser, and PE + laser followed by tumor harvest. All isolated tumor samples were fixed with 4 % formaldehyde and subsequently embedded in paraffin for further processing. The experiment details IHC staining of HIF-1α, CD-31, PCNA and TUNEL/PI double staining were illustrated in Supporting Information.

2.12 RNA extraction and data analysis
The experiments were performed in triplicate. Total RNA was extracted from the MDA-MB-231 using TRIzol reagent (Invitrogen) and RNeasy Mini Kit (Qiagen). The details for experiment and calculation are shown in Supporting Information.

2.13 Statistical analysis. Data represents mean ± SD from certain independent experiments, each performed in three replicates. Statistical comparisons were performed using GraphPad software 7. Differences between two groups were e calculated tested by a student's t-test. Reported p-values: ** $P < 0.05$ and *$P < 0.01$ were illustrated as significant difference between groups.

3. Results and Discussions
3.1. Preparation and characterization of PAuE, PAu and PE. AuNCs were synthesized *via* galvanic replacement reaction according to our previous report.[47] To improve the encapsulation efficiency of

AuNCs into Mal-PEG-PLGA , hydrophobic dodecanethiol (Dod)-decorated AuNCs (Dod@AuNCs) were firstly prepared by conjugation of Dod onto the surface of AuNCs with thiol group. To achieve the synergistic PTT and chemotherapy, MAL-PEG-PLGA@AuNCs/EGCG were obtained by encapsulating Dod@AuNCs and EGCG into MAL-PEG-PLGA polymer using nanoprecipitation method.[57] HS-iRGD peptides were attached to the surface of NPs by melamine-thiol interaction to obtain the targeted iRGD-PEG-PLGA@AuNC/EGCG (PAuE).[58] The control NPs, including non-targeting cysteine-modified Mal-PEG-PLGA-encapsulated AuNC and EGCG (CAuE), iRGD-modified Mal-PEG-PLGA-encapsulated AuNCs (PAu), iRGD-modified Mal-PEG-PLGA-encapsulated EGCG (PE) and Mal-PEG-PLGA NPs (BP) were also prepared. The chemical properties of each NP are shown in Table 1. A slight difference in particle sizes was observed by dynamic light scattering (DLS) measurements, ranging from 135-140 nm, indicating that the encapsulation of AuNCs and EGCG does not affect the size of Mal-PEG-PLGA NPs. Alternatively, the significant increase of zeta potential of PAuE (1.6 ± 0.5), PAu (1.8 ± 0.6) and PE (1.4 ± 0.3) compared to CAuE (-23.9 ± 1.4) indicated successful attachment of iRGD peptide on NPs surface. The DL % and EE % of PAuE NPs were estimated to be 2.27 % and 22.3 %, much higher than that of PE NPs (1.06 % of DL and 5.91% EE). The improved DL % and EE % is due to the hollow interior of AuNCs which facilitates drug loading.[49]

Representative transmission electron microscopy (TEM) images revealed Dod@AuNCs have uniform size distribution (Fig. 1a). A high-resolution TEM analysis confirmed (111) crystal plane with lattice spacing of 2.36 Å. TEM images also revealed shows the uniform spherical shape of PE NPs (Fig. 1b) and no obvious morphology change after entrapping AuNCs into the polymer core (Fig. 1c). The absorption spectra of AuNCs and PAuE indicated that the encapsulation process did not affect the optical properties of AuNCs (Fig. 1d). To further prove the successful surface modification, Fourier-transform infrared (FTIR) spectra of blank BP, free EGCG, CAuE and PAuE were conducted and compared (Fig. 1e). The characteristic peaks of Mal-PEG-PLGA (stretching bands at 3489 cm^{-1} for –OH and 2970 cm^{-1} for C–H, 1776 cm^{-1} for C=O of ester groups of PEG and PLGA) were present in the corresponding IR spectra. The IR spectra of EGCG displayed typical peaks at 3381 cm^{-1} for –OH groups adhere on aromatic rings, strong bands at 1691 cm^{-1} for the C=O functional group, and a series of bands in the range of 1400-1600 cm^{-1} correspond to the stretching of C-C bonds in EGCG benzene ring. The spectrum of CAuE indicated strong absorption bands at 3439, 2970, 1757 cm^{-1} and several bands in the region of 1400-1600 cm^{-1}, which correspond to the stretching vibration of EGCG and Mal-PEG-PLGA. The appearance of a classic peak at 1648 cm^{-1} is related to the C=O bond of amide groups of iRGD peptide in the spectrum of PAuE, which revealed iRGD peptide conjugation.

The drug release profile of EGCG from PAuE in two pH buffers (pH 7.4 and 5.8) was recorded by monitoring the drug concentration outside the bag using UV-vis absorption. The curve indicated an initial burst release followed by a slow and steady release to retain long circulation. The release of EGCG was observed to be about 20.3 ± 3.6 % and 70.5 ± 4.3 % over 24 hrs at pH 7.4 and pH 5.8, respectively (Fig. 1f). The increased release at lower pH is attributed to the degradation of PEGylation PLGA at mildly acidic conditions.[52,53] Under NIR irradiation, the amount of drug released from PAuE over 24 hrs showed a mild increase (49.5 ± 5.3 % and 85.0 % ± 6.3 %) compared to without laser irradiation at pH 7.4 and 5.8. Enhanced EGCG release triggered by laser irradiation is attributed to the heat generated from AuNCs which results in hyperthermia-induced collapse of NPs. After 3 days, the cumulative percentage of drug release from PAuE at pH 5.8 and under laser irradiation was 93.3 ± 2.0 %.

Table 1 Characterization of Mal-PEG-PLGA-encapsulated AuNCs and EGCG NPs using nanoprecipitation method. Data are mean ± SD, n = 3.

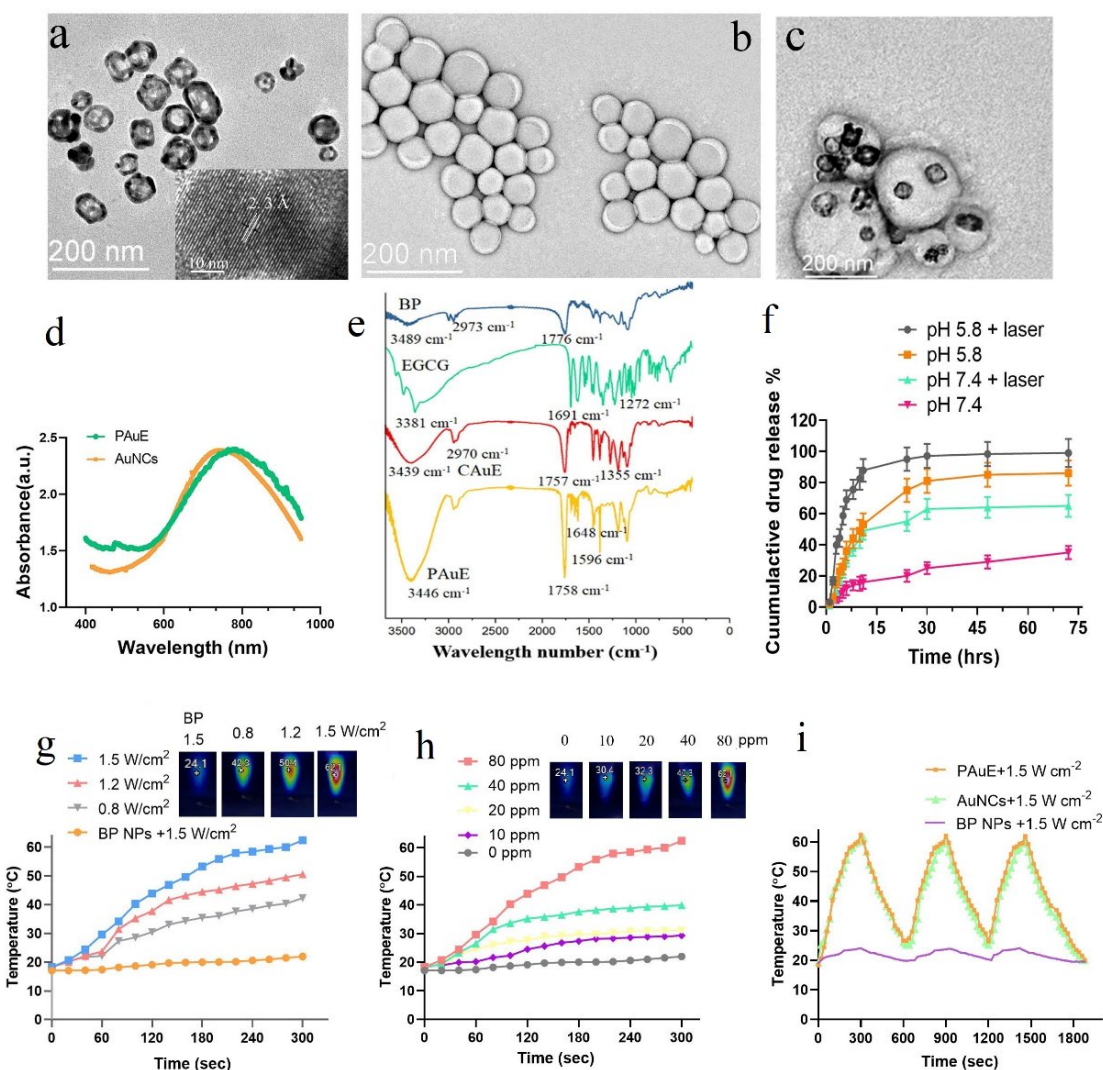| Nanoparticles	Particle size (nm)	Polydispersity index (PDI)	Zeta potential (mV)	DL (%)	EE (%)
BP	136.1 ± 2.7	0.11± 0.03	-33.4 ± 0.8	/	/
PAu	135.3 ± 3.3	0.09 ± 0.04	1.8 ± 0.6	/	/
PE	136.3 ± 2.4	0.12 ± 0.02	1.4 ± 0.3	1.06	5.91
CAuE	137.3 ± 3.4	0.22 ± 0.08	-23.9 ± 1.4	2.21	22.1
PAuE	140.1 ± 3.6	0.08 ± 0.07	1.6 ± 0.5	2.27	22.3

Fig. 1 Preparation and characterization of AuNCs and PAuE nanotheranostics. a TEM images of Dod@AuNCs with a high-resolution TEM image of the lattice planes (2.3 Å). b, c TEM images of PE and PAuE. d UV-vis-NIR spectra of AuNCs and PAuE. e FTIR spectra of BP, EGCG, CAuE and PAuE. f The *in vitro* EGCG release behavior of PAuE (n = 3) in different buffers with and without laser irradiation (1.2 W cm⁻², 3 mins) were recorded along with different time points. g Temperature response curves of BP and PAuE (40 ppm) after receiving 808 nm irradiation at different power densities (0.8, 1.2 and 1.5 W cm⁻²). h The photothermal effect of PAuE at various Au concentrations (0, 10, 20, 40 and 80 ppm) after laser irradiation (1.2 W cm⁻², 5 mins). i Multiple heating cycles of PAuE (40 ppm), AuNCs and BP upon NIR irradiation (1.5 W cm⁻², 5 mins).

3.2. Photothermal efficiency and photoacoustic property of the PAuE. To verify the photothermal ability of PAuE, photothermal-heating curves and the individual thermal image of PAuE were measured in different conditions. PAuE exhibited a power density-dependent photothermal-conversion efficiency upon laser irradiation (Fig. 1g). In contrast, BP exhibited negligible temperature change upon laser irradiation. On the other hand, the temperature of a higher concentration of PAuE increased in a dose-dependent manner upon laser irradiation (Fig. 1h). The photostability of PAuE was evaluated by testing three repeated heating-cooling cycles (laser on / off). The results indicated no obvious deterioration during the recycling, implying that PAuE has excellent photothermal stability (Fig. 1i). Moreover, the photothermal conversion efficiency (η) of PAu was estimated to be 32.6 % based on the formulas shown in supporting information (Figure S1). This high photothermal conversion efficiency and high photostability of PAuE provide a good foundation for MSOT imaging and PTT cancer therapy applications.
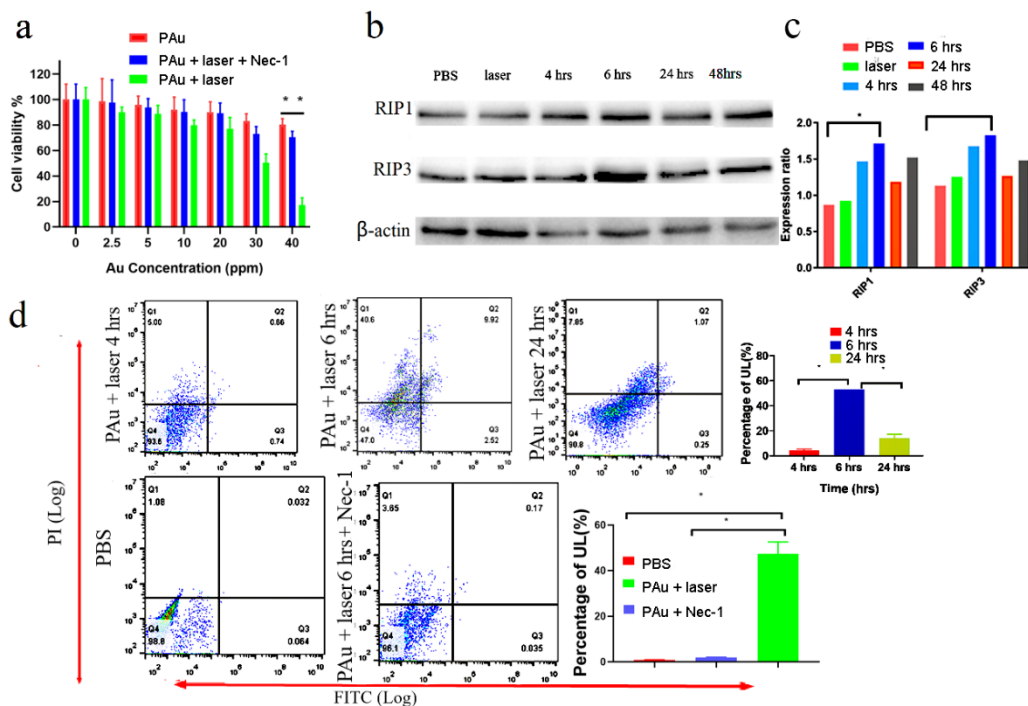
Fig. 2 Determination of cell death pathway after mild PTT treatment (808 nm, 1.2 W cm⁻², 3 mins) in MDA-MB-231 cells. a Cell viabilities after different treatments (PAu, PAu + laser and PAu + laser + Nec-1) for 24 hrs (n = 5). ** P< 0.05. b Presentative flow cytometry plots and quantitative analysis of the percentage of necroptotic cells of MDA-MB-231 cells receiving PAu + laser or PAu + laser + Nec-1 (40 ppm of AuNCs) treatment with different incubation time after laser irradiation (n = 3). c, d Western blot and semiquantitative analysis of necroptosis-related proteins in cells after PAu + laser treatment with different incubation time (4, 6, 24 and 48 hrs). RIP1: 76KD; RIP3: 57KD; β-actin: 42 KD. Data were represented as mean ± SD, each performed in five replicates.

3.3. *In vitro* cytotoxicity and necroptosis-related cell death induced by PAu. To address the mechanism of the cell death events from mild PTT, western blots and flow cytometry was carried out to test PAu + laser using human breast cancer MDA-MB-231 cells. There was a negligible effect on the cells even for with a concentration of 40 ppm of PAu, which verified its good biocompatibility, while a significant decrease was noticed in the PAu + laser group in a dose-dependent manner (Fig. 2a). Given those various extrinsic stimuli may trigger cell death in different manners, the cells were pre-treated with a necroptotic inhibitor, necrostatin-1 (Nec-1), to evaluate whether necroptosis dominates the programmed cell death. In the presence of PTT + Nec-1, the cytotoxicity of MDA-MB-231 cells decreased remarkably than that of the PTT-only group, with both at a higher dose, suggesting that necroptosis is the main cause of cell death. We then performed flow cytometry with annexin V/propidium iodide (PI) double staining to investigate the trend of necroptosis in a time-dependent way (Fig. 2b). Acknowledging that the signal of annexin V indicates an apoptotic process, we considered the cell population to fall in the upper left quadrant, the annexin V-negative (annexin V-) /PI-positive (PI +) portion, as an indicator for necroptosis. We noticed that 52.9 % of cells went through necroptosis at 6 hrs post-incubation after mild PTT (PAu + laser, reaching 45 °C), which was apparently higher than that of 4 hrs (4.0 %) and 24 hrs (14.0 %). No significant apoptotic events were observed in both 4 hrs (5.9 %) and 6 hrs (5.4 %) of incubation time, but apoptosis became dominant at 24 hrs (46.1%) (the upper row in Fig. 2b). The percentage of live, necroptotic and apoptotic cells is totally different at different incubation times, indicating that the cell death pathway inflicted from mild PTT of PAu is a time-dependent process that mainly goes through necroptosis at first followed by apoptosis. Nec-1 treatment was introduced before mild PTT, and the flow cytometry analysis showed a great reduction of the cell population at the upper left quadrant, validating necroptosis was highly involved in the mild PTT-induced cell death (the lower row in Fig. 2b).

In comparison to apoptosis, necroptosis is caspase-independent and the implementation of the necroptosis pathway is mainly related to the expression of proteins RIP1 and RIP3. We examined their expression levels and found that both were highly expressed at 6 hrs post-incubation after mild PTT (Fig. 2c and 2d). Notably, the 6 hrs group exhibited significant RIP1 and RIP3 expression compared to the 4 and 24 hrs marks, revealing that the necroptosis phenomenon reaches its maximum at this time point. Also, the lower expression of RIP1 and RIP3 at other time points may result from the delayed apoptosis (24 hrs after mild PTT), given that necroptosis is often activated by apoptosis inducers such as tumor necrosis factor (TNF). In line with these observations, we began our investigations in the switch between necroptosis and apoptosis.

3.4. *In vitro* cytotoxicity and necroptosis and apoptosis-related cell death induced by PAuE.
The synergistic therapeutic effect of PAuE with or without laser irradiation was evaluated on MDA-MB-231 cell lines by CCK8 assays (Fig. 3a and b). With the presence of laser exposure (808 nm, 1.2 W cm^{-2}, 5 min), the cytotoxicity of PAuE enhanced 3.6 folds than the laser absent group at the highest dose. Meanwhile, the IC$_{50}$ (based on Au concentration) of PAuE significantly decreased from 40.3 ppm to 28.4 ppm in the presence of laser exposure, demonstrating an efficient photothermal therapeutic effect *in vitro*. Concomitantly, the IC$_{50}$ (based on EGCG concentration) of PAuE also decreased from 98.3 μg/ml for EGCG (laser absent) to 74.5 μg/ml for EGCG (laser present) revealed that mild PTT/chemotherapy can reach a superior anti-tumor efficacy (Fig. 3a). Besides, the cell viability of PAuE was significantly lower than PAu, revealing the release of EGCG from the NPs led to higher cytotoxicity than EGCG-free NPs, regardless of NIR laser irradiation. With 50 μg/ml EGCG introduced, the cell viability of PAuE + laser was down to 15.7 %, whereas PAu landed around 85.2 % even at higher dose level (40 ppm Au) showing no obvious toxicity (Fig. 3b). All the cell viability studies showed convincing evidence that PAuE is biologically compatible. Despite the enhanced EGCG release kinetics following laser irradiation in an acidic condition, we explored the feasibility of PE as a chemotherapeutic agent. An *in vitro* cytotoxicity test was done with PE, showing the cytotoxicity of PE on MDA-MB-231 cells increased in a dose-dependent manner regardless of laser exposure (Figure S2). To visualize the synergistic efficacy of PAuE *in vitro*, a calcein-AM (green FL, live cells) and PI (red FL, dead cells) costaining study was performed. It was clear from these fluorescence images that the majority of cells incubated with PAuE + laser showed much more red fluorescence than cells that received other treatments, indicating more cells were dead (Fig. 3c).

We also observed that apoptosis is a major mechanism for PE to destroy breast cancer, which is similar to previous studies (Figure S3). The expressions of a series of apoptosis-associated proteins, including Bcl-2 and cleaved caspase 3, were assessed to verify the mechanism that PE and free EGCG caused cell death (Figure S4). A single treatment *via* PE that shifted the expression level of Bcl-2 in favor of apoptosis requires a high dosage of EGCG (100 μg/ml).

With AuNCs installation and laser exposure (50 μg/ml and 40 ppm for EGCG and Au concentration, laser < 49 °C), we noticed a synergistic anti-tumor effect in which PAuE significantly activated apoptosis with increased expression of caspase (Fig. 3d).

TNF-1α would induce the activation of PARP1 *via* DNA damage leading to ATP depletion and subsequently triggering necroptosis [59]. PAPR1 is a nuclear enzyme that is activated by DNA damage, generating plenty of NAD+, resulting in large amount ATP depletion. Herein, PARP1 acts as cross regulators presumably between necroptosis and apoptosis by regulating ATP levels. The downstream manifestations of PARP1 often connect with death receptors such as RIP1 and RIP3 [26]. To further confirm the necroptosis mechanism in-depth, the expression level of two critical kinases, RIP1 and RIP3 was studied in MDA-MB-231(Fig. 3d and 3e). The activity of RIP1 and RIP3 are highly expressed in the cells treated with PAu + laser and PAuE + laser compared to PBS, laser only and PE NPs. Mitochondrial impairment *via* activation of PARP1 induced by necroptosis involves the change in the mitochondrial membrane permeability. PAuE also exhibited slight enhancement in the expression of pro-caspase 3 and cleaved caspase to activate the apoptosis in cancer cells compared to PE with the same EGCG concentration. We also performed western blot analysis on another pair of the proteins Bcl-2/Bax that the expression ratio is crucial to affect apoptosis. The moderate change in expression level of Bcl-2/Bax of PAuE + laser would benefit cell apoptosis at a EGCG concentration of 50 μg/ml. Previous studies reported on potential apoptosis induction in breast cancer cells by decreasing Bcl-2/Bax expression when treated with EGCG [60]. Our results are in line with the above observations, owing to these characteristics endowed by PAuE + laser with combined actions of dual necroptosis and apoptosis induction and increased expression of PARP1. The schematic of the mechanism of PAuE + laser treatment leading to cell death (Fig. 3f). We hypothesized that necroptosis maybe dominates the pathway for cell death after PAuE + laser in 6 hrs post-incubation. Nevertheless, the expression of pro-caspase does not change much, indicating the apoptosis takes small portion in cell death at this time point.
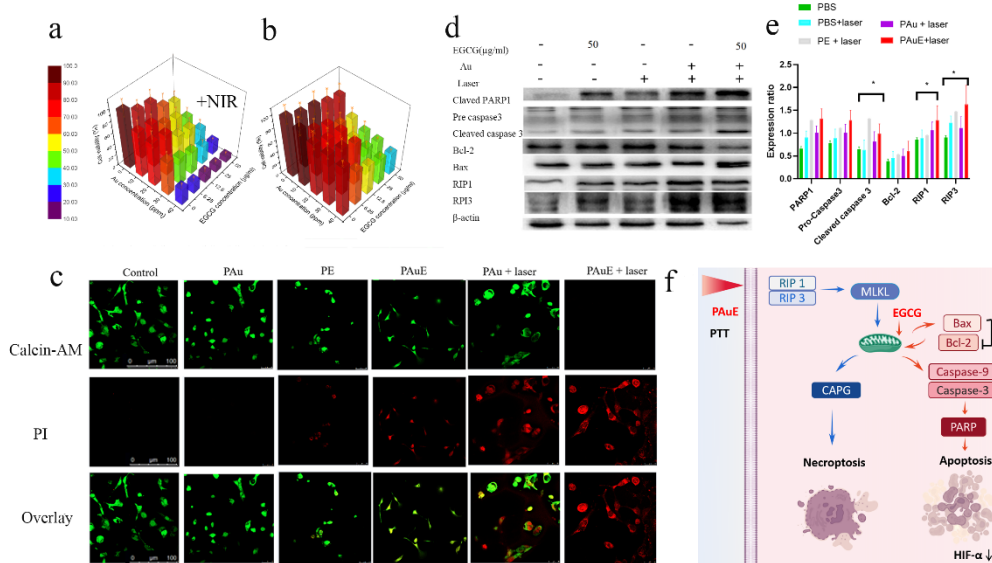
Fig. 3 a, b Cell viability upon treatment with PAuE, PAu and PE for 24 hrs with (a) and without (b) laser irradiation (808 nm, 1.2 W cm^{-2}, 3 mins). *P < 0.1, ** P < 0.05. Data represent mean ± SD from three independent experiments, each performed in five replicates. c CLSM images of live and dead MDA-MB-231 cells with Calcein AM /PI staining and different treatments. Scale bar is 100 μm. d Western blot analysis of apoptosis/necroptosis-associated proteins after 24 hrs treatment with PBS, PBS + laser, PE, PAu + laser, and PAuE + laser. (40 ppm of AuNCs; 50 μg/ml of EGCG; laser irradiation: 808 nm, 1.2 W cm^{-2}, 3 mins). (e) Corresponding semiquantitative result. (f) Signaling pathway of anticancer mechanism of PAuE + laser.

3.5. *In vivo* distribution of PAuE tracked by MSOT imaging. To test the capability of targeting PAuE and non-targeting CAuE for MSOT imaging *in vivo*, we performed MSOT images analysis to reveal the real time biodistribution of PAuE at the tumor site and other organs in the MDA-MB-231 orthotropic tumor model. In our present study, *in vivo* MSOT signal from AuNCs can be visualized in the tumor at 6 hrs post-injection of PAuE (30 mg kg^{-1}, based on AuNCs weight; 5 mg kg^{-1} based on the EGCG weight) (Fig. 4a). The images showed a local distribution in tumor of the AuNCs over 24 hrs which gradually decreased and eventually disappeared after 72 hrs. Besides, 3D whole-body (excluding head, neck and tail) MSOT images demonstrated that PAuE was observed in other organs, including liver, spleen and lungs at different time points (Fig. 4b). The quantified MSOT intensities in the tumor, liver, and spleen were recorded at different points (Fig. 4c). The gradual decrease of PAuE accumulation in the tumor and main organs were attributed to renal clearance *via* liver and spleen after 72 hrs. In comparison, no obvious accumulation of CAuE was found in the tumor region after intravenous administration (Figure S5a). However, the liver and spleen retained high uptakes at 24 hrs post-injection of CAuE, which was much stronger than that of PAuE (Additional file 1: Figure S5b and c). It indicated that iRGD played a pivotal role in enhancing cellular uptake in the tumor region. The utilization of distinct LSPR characteristics of AuNCs *via* MSOT imaging provides a capacity for reflecting the optoacoustic signal intensities of the PAuE distribution *in vivo* at varied times.
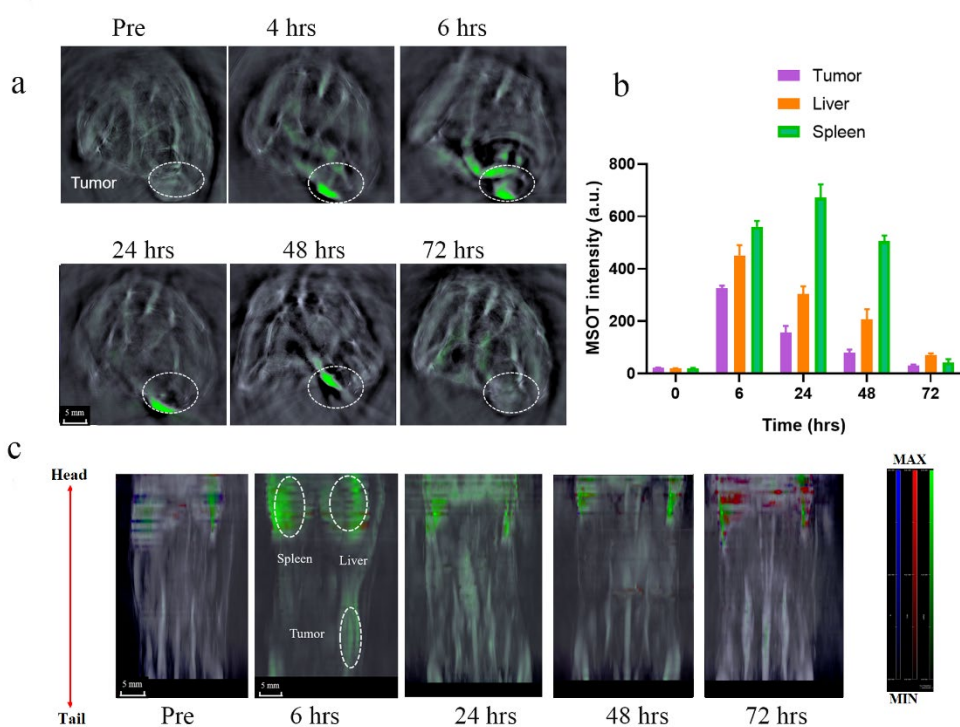
9

Fig. 4 MSOT images of mice bearing MDA-MB-231 tumor receiving PAuE NPs. a Cross-sectional MSOT images of MDA-MB-231 tumor for a tumor-bearing mouse at a varied time upon injection of PAuE NPs. The region of the tumor is marked with white curves (n = 3), scale bar (5 mm). b Relative MSOT signal intensity of liver, spleen and tumor at different time points upon injection of PAuE. c *In vivo* representative z-stack orthogonal MSOT maximal intensity projection (MIP) images of tumor after tail vein injection of PAuE (AuNCs concentration: 30 mg/kg) at different time points (n = 3). The images were combined with both signals from PAuE (in color) and typical cross-sectional MSOT images (with a background in gray color), scale bar (5 mm).

3.6. *In vivo* antitumor activity and mechanism studies. With the promising *in vitro* cytotoxicity studies and the synergistic induction of necroptosis and apoptosis, we further extended our interests in the therapeutic efficacy of mild PTT/EGCG combined therapy *in vivo*. Twenty-four MDA-MB-231 orthotopic tumor-bearing mice were randomly divided into six treatment groups: (1) PBS, (2) PBS + laser, (3) PE, (4) PAu + laser, (5) PAu, and (6) PAuE + laser. Tumor inhibition, body weights and survival rates were assessed for addressing the therapeutic outcomes. MSOT images depicted the maximum accumulation of PAuE inside tumor at 6 hrs post-injection. Laser irradiation (808 nm) was employed after 6 hrs post-injection of nanotheranostics to assess the synergistic therapeutic effect of mild PTT and EGCG (Fig. 5a). Notably, the tumor temperature was found to reach 49 °C after 5 mins of laser exposure in the PAuE + laser group (Fig. 5b). In contrast, the control group exhibited minimal temperature change (34 °C to 39°C), demonstrating the localized heating effect of PAuE after laser irradiation. The mice treated with PAu showed a moderate inhibition effect on the tumor growth compared to the control groups (PBS or PBS + laser). On the contrary, the treatment of PE (green line) and PAu + laser (red line) both exhibited growth inhibition effects, revealing their anti-tumor activity respectively. More importantly, PAuE + laser (black line) exhibited significantly higher anti-tumor inhibition efficacy than other groups, demonstrating the combined effect of mild PTT and chemotherapy. PAuE + laser group achieved significant inhibition in tumor growth, followed by the groups of PE, PAu + laser, PAu, PBS (Fig. 5d, and Figure S6). To investigate systemic toxicity on the mice, we continue to monitor the change in body weight in all groups during the treatment period, confirming no significant body weight fluctuation to reveal the low toxicity of PAuE + laser (Fig. 5h). Moreover, no obvious tissue damages were present in main organs (liver, heart, kidney) in all experimental groups measured by the H&E staining assay; this result is consistent with our *in vivo* toxicity tests (Figure S7). Furthermore, Kaplan-Meier survival curves were used to assess the therapeutic efficacy. During the whole treatment process, PAuE + laser exhibited a gradual increase in survival rate, where 100 % of the mice survived. With PBS or PBS + laser as control groups, all mice died as an effect of tumor metastasis whereas treatment with PE, PAu + laser rescued only 40 % and 60 % of mice. As revealed in the survival curves, PAuE + laser could efficiently increase the lifespan of mice bearing malignant tumors.
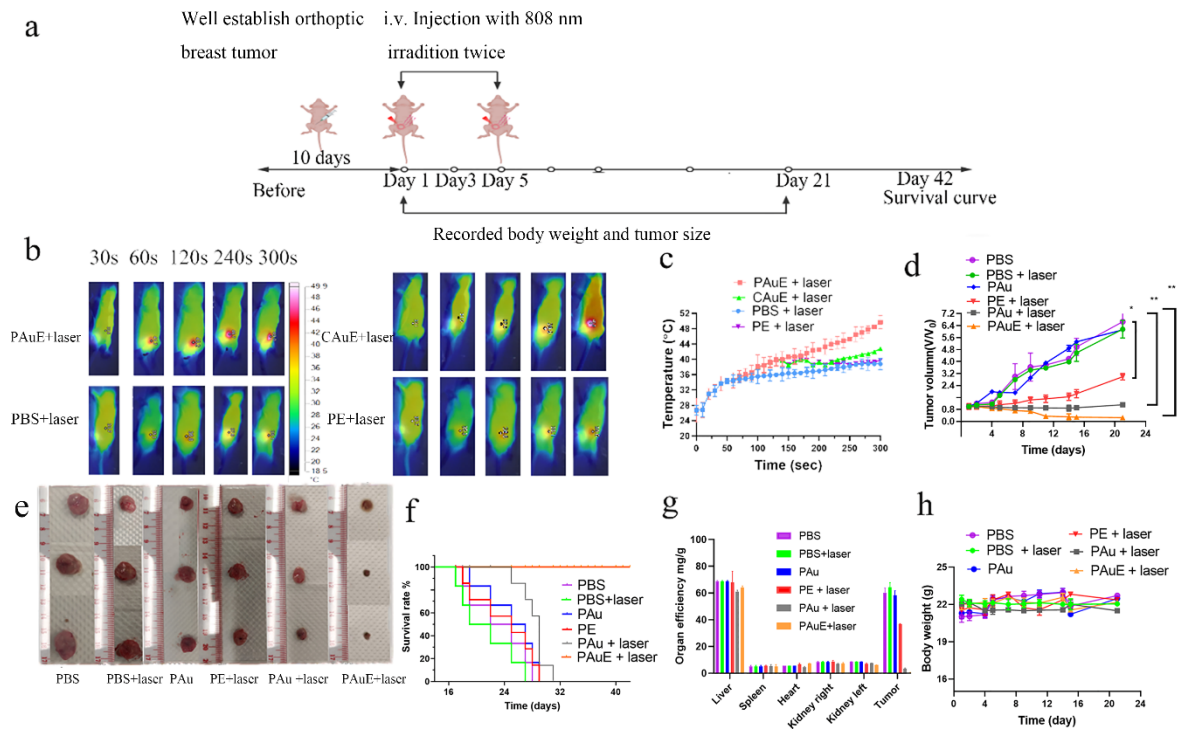
Fig. 5 *In vivo* antitumor effects of the NPs in the MDA-MB-231 tumor-bearing nude mice, showing that PAuE + laser group has the best synergistic therapy performance. a Schematic illustration of the establishment of orthotopic breast model and treatment with PAuE nanoparticles under 808 nm laser irradiation at the (5 mg/kg) concentration, guided by MSOT imaging. b Infrared thermal images of tumor-bearing mice. c Temperature changes of tumor regions intravenously injected with 200 μL of PBS and PAuE (5 mg/kg EGCG, 30 mg/kg AuNCs) and CAuE + laser (5 mg/kg EGCG, 30 mg/kg AuNCs), PE+ laser (5 mg/kg EGCG) at 6 hrs post-injection subject NIR laser irradiation (1.2 W cm^{-2}, 5 mins) (n = 4). d Tumor growth curve of various treatment groups (n = 4). e Images of tumors receiving all treatment groups after the 21 days of the experiment. f, g Survival curve and organ efficiency of tumor-bearing mice treated by various groups during 42 days (n = 5). h Body weight change of mice after various treatments at the duration of therapy (n = 4).

Current studies demonstrated that EGCG induces anti-cancer effect by blocking the activity of mitogen-activated protein kinases (MAPKs), IGF/IGF-I receptor, NFkB and HIF-1α pathways.[54,61] In addition, HIF-1α is a critical mediator of hypoxia-induced apoptosis in the intralesional tumor and the expression level of the HIF-1α might affect the prognosis of cancer treatment.[62] Therefore, we present a further study to test whether PAuE nanoplatform induced apoptosis through suppression of HIF-1α in MDA-MB-231 cells. The results indicated that PE and PAuE both inhibited the expression level of HIF-1α upon laser irradiation in MDA-MB-231 cells (Figure S8), which holds a promising inhibition effect on the growth and proliferation of breast cancer cells *via* the inhibition of HIF-1α-associated apoptotic signal. In addition, PE showed stronger downregulated expression of HIF-1α than free EGCG, possibly due to the sustained release and enhanced upake of the nanoplatform.[56] Also, the expression of HIF-1α in PAuE + laser group is much lower than that of PE or PAu + laser alone (Fig. 6a), suggesting the combination of mild PTT and chemotherapy enhanced the inhibition of HIF-1α activation. Immunohistochemical (IHC) staining for HIF-1α of tumor tissue showed that HIF-1α protein expression was mainly localized in the nuclei of tumor cells, with

some in the cytoplasm (Fig. 6a). The IHC staining intensity was measured as the optical density determined by Image J and a detailed calculation process is shown Supporting Information.

The anti-tumor effects of treatment groups were also investigated with histopathology analysis via hematoxylin-eosin (H&E) staining, IHC assay with CD31 and PNAC staining and immunofluorescent study of tumor tissues (Fig. 6b). Apparent shrinkage of cell morphology and breakdown of tumor tissue were noticed in the PAuE + laser group compared with control, indicating the effective tumor suppression effect. IHC assay with CD31 and proliferating cell nuclear antigen (PCNA) staining demonstrated that tumor angiogenesis and cancer cell proliferation were significantly reduced in the tumors in the PAuE NPs + laser group. Moreover, terminal deoxynucleotidyl transferase dUTP nick end labelling (TUNEL) assay and PI double staining were performed on tissue sections to study the proportion of apoptotic (green fluorescence) or necroptotic (red fluorescence) cell death in the treatment groups. It revealed that the PE group contributes to a higher apoptosis rate of tumor cells compared to the others, indicating that apoptosis was the major occurrence for tumor growth inhibition for the PE group. Nevertheless, the tumor tissue of PAu + laser

11

group exhibited primarily red fluorescence, indicating the evidence of necroptotic cell death which might result in lower levels of green fluorescence in only mild PTT treatment tissue sections. Besides, the high percentage of TUNEL and PI-positive nuclei could be observed in the PAuE + laser group, indicating that apoptosis and necroptosis might induce the primary pathways of PAuE + laser leading to cell death.
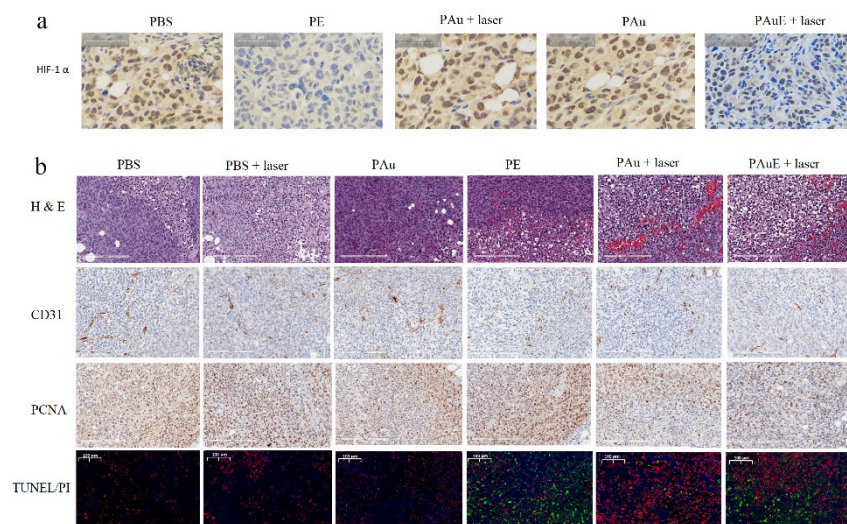

Fig. 6 Validation of cell death pathway via IHC. a Representative images and quantities of IHC staining of HIF-1α in tumor tissue (Scale bars 50 μm). b Histological observation of the tumor tissues with H&E staining (Scale bars 200 μm); IHC staining of angiogenic neovessels (CD31) and PCNA; and detection of apoptosis by TUNEL assay and necroptosis by PI staining in tumor tissues from different treatments. Cell nuclei (blue), apoptotic spots (green) and necroptotic spots (red) (Scale bars 100 μm). (40 ppm of AuNCs; 50 μg/ml of EGCG; laser irradiation: 808 nm, 1.2 W cm^{-2}, 3 mins).

3.7 Gene expression studies

To evaluate the combined effect of mild PTT and chemotherapy on certain cell death responses in human MDA-MB-231 cells, the expressions of necroptosis/apoptosis-related genes treated with PAuE upon laser irradiation was studied by RNA sequencing. Using KEGG analysis, our findings illustrated the DEGs (differentially expressed genes)-enriched pathways which showed that the altered genes were part of the core network of genes driving RCD in cancer (Fig. 7a). Extracting DEGs information from KEGG pathways of interest, we showed that PAuE + laser activated a set of unique gene expression responses in MDA-MB-231 cells. 10 and 6 genes exhibited up- and downregulation, respectively, in a total of 19 differently regulated genes of PAuE + laser group; the expression in the other 3 genes were unchanged (Fig. 7b). Besides, the gene expression pattern for PAu + laser group was similar to PAuE + laser group. Interestingly, upregulated genes include BCL2L14, and TNF α, which exert proapoptotic activity and are also involved in triggering necroptosis. MDA-MB-231 is refractory to apoptosis thus the upregulation of FAS and TNFAIP2 genes in the TNFα pathway might be related to the induction of necroptosis cross-talking.

BCL2 and receptor-interacting protein kinase 1 (RIPK1), in particular RIP1 and RIP3, act as messengers to induce necroptosis (Scheme1). As a result, PAuE + laser evoked more cell death upon laser irradiation and slightly initiated caspase-intendent cell death mechanisms in apoptotic impervious cells (Fig. 7b). The results of the transcriptomic analysis for PAuE + laser showed a significant change in the expression of effectors in different components of necroptosis machinery like TNF α and RIPK1. This situation demonstrated a fine crosstalk among the RCD pathway. Not surprisingly, autophagy-related genes (ATG16L2) and ATG3, which could induce autophagy-related cell death, and key factors related to necroptosis signalling (PARP1, RIPK1) were upregulated upon irradiation in PAuE treated gro
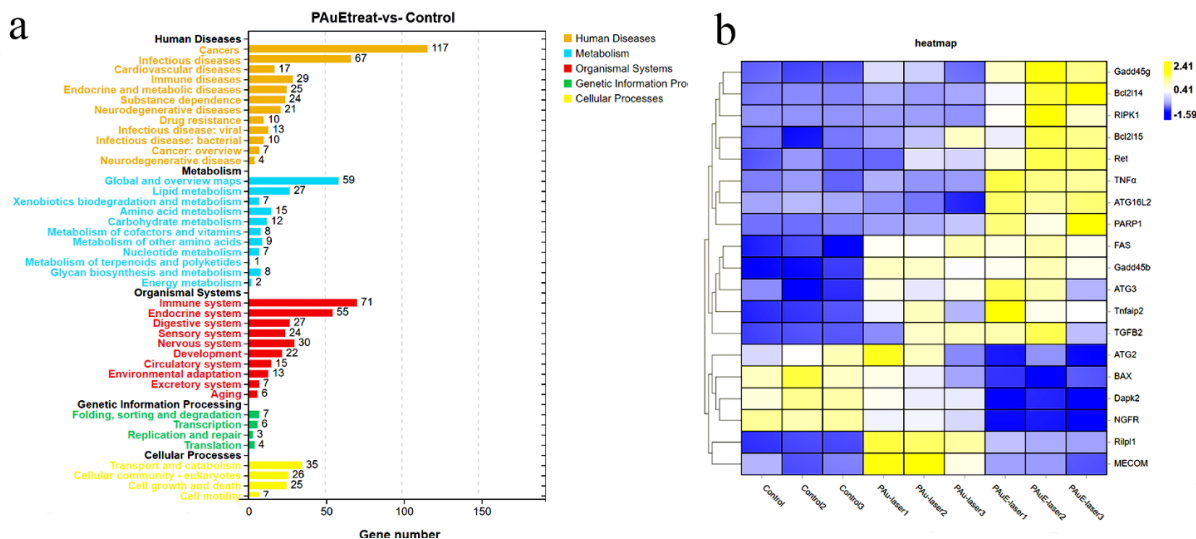
Fig. 7 Cell death pathway focused gene expression analyses in MDA-MB-231. a Kyoto Encyclopedia of Genes and Genomes (KEGG) enrichment analysis of PAuE + laser. The enrichment analysis implies the number of all genes in a certain enrichment pathway. b A heat map shows apoptosis/necroptosis-related differentially expressed gene. Color intensity represents the degree of expression value of this gene after standardized treatment in each sample. Relative expression levels are shown in yellow (upregulation) and blue (downregulation).

4. Conclusion

In summary, an original PAuE nanoplatform integrating the facilitation of mild PTT, enhanced drug-loading, *in vivo* tracking, and tumor-targeting functions into a single formulation was fabricated. PAuE could serve as an effective nanotheranostic agent to enable MSOT-guided synergistic mild PTT and chemotherapy. Upon laser irradiation, AuNCs generated a moderate thermal escalation to explore the necroptosis and apoptosis mechanisms by adjusting the incubation time. A combination of mild PTT and EGCG in the form of a nanoplatform greatly enhances its *in vitro* and i*n vivo* therapeutic efficacy through evoking necroptosis at an early stage followed by apoptosis in a later stage. Targeting the necroptosis pathway by nanoparticles via PTT is emerging as an effective approach in cancer therapy, in which inducing apoptosis in later chemotherapy gains a potential advantage to bypass the apoptosis resistance and maintain antitumor immunity.[63] Besides, the other potential advantages of the cell death pathway switch include the minimized risk of the tumor recurrence. More importantly, *in vivo* experiments have confirmed that mild PTT promotes the release of EGCG which is capable of enhancing apoptosis by inhibition of HIF-1α expression. The synergistic induction of necroptosis and apoptosis by combining mild phototherapy and chemotherapy is convincing by the gene expression studies. The results provided insights on efficient anticancer response receiving PAuE + laser in view of precision medicine applications.

ASSOCIATED CONTENT

AUTHOR INFORMATION
Corresponding Author
*Yan-Juan Gu - Department of Applied Biology and Chemical Technology, The Hong Kong Polytechnic University, Hung Hom, Hong Kong, China; Email: yanjuan.gu@polyu.edu.hk

*Liang-ting Lin - Department of Health Technology and Informatics, The Hong Kong Polytechnic University, Hung Hom, Hong Kong, China; Email: lt.lin@polyu.edu.hk

*Wing-Tak Wong - Department of Applied Biology and Chemical Technology, The Hong Kong Polytechnic University, Hung Hom, Hong Kong, China; Email: w.t.wong@polyu.edu.hk

Author Contributions
‡These authors contributed equally.

Notes
The authors declare no conflict of interest.

ABBREVIATIONS
AuNCs, gold nanocages; EGCG, epigallocatechin gallate; MSOT, multispectral optoacoustic tomography; PTT, photothermal therapy; PTA, photothermal agent; Hsps, shock proteins; HIF-1α, hypoxia-inducible factor-1; RCD, regulated cell death; RIP, receptor-interacting protein; MLKL mixed lineage kinase domain-like protein; PDT, photodynamic therapy; HS-iRGD, cys-modified cyclic iRGD (Cys-Cys–Arg–Gly–Asp–Lys–Gly–Pro–Asp–Cys, disulfide bridge C2-C10, CCRGDKGPDC, peptide; PAuE, iRGD-PEG-PLGA/AuNCs/EGCG NP; TEM, transmission electron microscope; DLS, dynamic light scattering; PBS, phosphate buffer solution; H&E, hematoxylin and eosin; ROI, region of interest; TNF, tumor necrosis factor; MAPKs, mitogen-activated protein kinases; IHC, immunohistochemical staining; PCNA, proliferating cell nuclear antigen; autophagy-related genes ATG16L2; differentially expressed genes, DEG ; TUNEL, terminal deoxynucleotidyl transferase dUTP nick end labelling.

REFERENCES
(1) Chen, P.; Ma, Y.; Zheng, Z.; Wu, C.; Wang, Y.; Liang, G. Facile Syntheses of Conjugated Polymers for Photothermal Tumour Therapy. *Nat. Commun.* **2019**, *10* (1), 1192.

(2) Liu, Y.; Bhattarai, P.; Dai, Z.; Chen, X. Photothermal Therapy and Photoacoustic Imaging via Nanotheranostics in Fighting Cancer. *Chem. Soc. Rev.* **2019**, *48* (7), 2053–2108.

(3) Xiong, R.; Hua, D.; Van Hoeck, J.; Berdecka, D.; Léger, L.; De Munter, S.; Fraire, J. C.; Raes, L.; Harizaj, A.; Sauvage, F.; Goetgeluk, G.; Pille, M.; Aalders, J.; Belza, J.; Van Acker, T.; Bolea-Fernandez, E.; Si, T.; Vanhaecke, F.; De Vos, W. H.; Vandekerckhove, B.; van Hengel, J.; Raemdonck, K.; Huang, C.; De Smedt, S. C.; Braeckmans, K. Photothermal Nanofibres Enable Safe Engineering of Therapeutic Cells. *Nat. Nanotechnol.* **2021**, *16* (11), 1281–1291.

(4) Ma, Q.; Sun, X.; Wang, W.; Yang, D.; Yang, C.; Shen, Q.; Shao, J. Diketopyrrolopyrrole-derived Organic Small Molecular Dyes for Tumor Phototheranostics. *Chinese Chem. Lett.* **2022**, *33* (4), 1681–1692.

(5) Zhang, X.; Du, J.; Guo, Z.; Yu, J.; Gao, Q.; Yin, W.; Zhu, S.; Gu, Z.; Zhao, Y. Efficient Near Infrared Light Triggered Nitric Oxide Release Nanocomposites for Sensitizing Mild Photothermal Therapy. *Adv. Sci.* **2019**, *6* (3), 1801122.

(6) Zhao, P.; Jin, Z.; Chen, Q.; Yang, T.; Chen, D.; Meng, J.; Lu, X.; Gu, Z.; He, Q. Local Generation of Hydrogen for Enhanced Photothermal Therapy. *Nat. Commun.* **2018**, *9* (1), 4241.

(7) Kumar, S.; Stokes, J.; Singh, U. P.; Scissum Gunn, K.; Acharya, A.; Manne, U.; Mishra, M. Targeting Hsp70: A Possible Therapy for Cancer. *Cancer Lett.* **2016**, *374* (1), 156–166.

(8) Wang, S.; Tian, Y.; Tian, W.; Sun, J.; Zhao, S.; Liu, Y.; Wang, C.; Tang, Y.; Ma, X.; Teng, Z.; Lu, G. Selectively Sensitizing Malignant Cells to Photothermal Therapy Using a CD44-Targeting Heat Shock Protein 72 Depletion Nanosystem. *ACS Nano* **2016**, *10* (9), 8578–8590.

(9) Chu, K. F.; Dupuy, D. E. Thermal Ablation of Tumours: Biological Mechanisms and Advances in Therapy. *Nat. Rev. Cancer* **2014**, *14* (3), 199–208.

(10) Rundqvist, H.; Johnson, R. S. Tumour Oxygenation: Implications for Breast Cancer Prognosis. *J. Intern. Med.* **2013**, *274* (2), 105–112.

(11) Garheng Kong, R. D. B. and M. W. D. Characterization of the Effect of Hyperthermia on Nanoparticle Extravasation from Tumor Vasculature. *Cancer Res. 61* (7), 3027–3032.

(12) Wang, J.; Liu, J.; Liu, Y.; Wang, L.; Cao, M.; Ji, Y.; Wu, X.; Xu, Y.; Bai, B.; Miao, Q.; Chen, C.; Zhao, Y. Gd-Hybridized Plasmonic Au-Nanocomposites Enhanced Tumor-Interior Drug Permeability in Multimodal Imaging-Guided Therapy. *Adv. Mater.* **2016**, *28* (40), 8950–8958.

(13) Zhan, C.; Huang, Y.; Lin, G.; Huang, S.; Zeng, F.; Wu, S. A Gold Nanocage/Cluster Hybrid Structure for Whole-Body Multispectral Optoacoustic Tomography Imaging, EGFR Inhibitor Delivery, and Photothermal Therapy. *Small* **2019**, *15* (33), 1900309.

(14) Sun, H.; Su, J.; Meng, Q.; Yin, Q.; Chen, L.; Gu, W.; Zhang, Z.; Yu, H.; Zhang, P.; Wang, S.; Li, Y. Cancer Cell Membrane-Coated Gold Nanocages with Hyperthermia-Triggered Drug Release and Homotypic Target Inhibit Growth and Metastasis of Breast Cancer. *Adv. Funct. Mater.* **2017**, *27* (3), 1604300.

(15) Wang, L.; Yu, Y.; Wei, D.; Zhang, L.; Zhang, X.; Zhang, G.; Ding, D.; Xiao, H.; Zhang, D. A Systematic Strategy of Combinational Blow for Overcoming Cascade Drug Resistance via NIR-Light-Triggered Hyperthermia. *Adv. Mater.* **2021**, *33* (20), 2100599.

(16) Wang, L.; Lin, X.; Wang, J.; Hu, Z.; Ji, Y.; Hou, S.; Zhao, Y.; Wu, X.; Chen, C. Novel Insights into Combating Cancer Chemotherapy Resistance Using a Plasmonic Nanocarrier: Enhancing Drug Sensitiveness and Accumulation Simultaneously

with Localized Mild Photothermal Stimulus of Femtosecond Pulsed Laser. *Adv. Funct. Mater.* **2014**, *24* (27), 4229–4239.

(17) Li, W.; Peng, J.; Tan, L.; Wu, J.; Shi, K.; Qu, Y.; Wei, X.; Qian, Z. Mild Photothermal Therapy/Photodynamic Therapy/Chemotherapy of Breast Cancer by Lyp-1 Modified Docetaxel/IR820 Co-Loaded Micelles. *Biomaterials* **2016**, *106*, 119–133.

(18) He, P.; Wang, X.-X.; Cai, Y.-Z.; Shu, J.-C.; Zhao, Q.-L.; Yuan, J.; Cao, M.-S. Tailoring Ti 3 C 2 T x Nanosheets to Tune Local Conductive Network as an Environmentally Friendly Material for Highly Efficient Electromagnetic Interference Shielding. *Nanoscale* **2019**, *11* (13), 6080–6088.

(19) Wang, Z.; Li, S.; Zhang, M.; Ma, Y.; Liu, Y.; Gao, W.; Zhang, J.; Gu, Y. Laser-Triggered Small Interfering RNA Releasing Gold Nanoshells against Heat Shock Protein for Sensitized Photothermal Therapy. *Adv. Sci.* **2017**, *4* (2), 1600327.

(20) Chang, M.; Hou, Z.; Wang, M.; Li, C.; Lin, J. Recent Advances in Hyperthermia Therapy-Based Synergistic Immunotherapy. *Adv. Mater.* **2021**, *33* (4), 2004788.

(21) Chen, Q.; Hu, Q.; Dukhovlinova, E.; Chen, G.; Ahn, S.; Wang, C.; Ogunnaike, E. A.; Ligler, F. S.; Dotti, G.; Gu, Z. Photothermal Therapy Promotes Tumor Infiltration and Antitumor Activity of CAR T Cells. *Adv. Mater.* **2019**, *31* (23), 1900192.

(22) Deng, X.; Shao, Z.; Zhao, Y. Solutions to the Drawbacks of Photothermal and Photodynamic Cancer Therapy. *Adv. Sci.* **2021**, *8* (3), 2002504.

(23) Su, Z.; Yang, Z.; Xie, L.; DeWitt, J. P.; Chen, Y. Cancer Therapy in the Necroptosis Era. *Cell Death Differ.* **2016**, *23* (5), 748–756.

(24) Martens, S.; Bridelance, J.; Roelandt, R.; Vandenabeele, P.; Takahashi, N. MLKL in Cancer: More than a Necroptosis Regulator. *Cell Death Differ.* **2021**, *28* (6), 1757–1772.

(25) Gong, Y.; Fan, Z.; Luo, G.; Yang, C.; Huang, Q.; Fan, K.; Cheng, H.; Jin, K.; Ni, Q.; Yu, X.; Liu, C. The Role of Necroptosis in Cancer Biology and Therapy. *Mol. Cancer* **2019**, *18* (1), 100.

(26) Tang, D.; Kang, R.; Berghe, T. Vanden; Vandenabeele, P.; Kroemer, G. The Molecular Machinery of Regulated Cell Death. *Cell Res.* **2019**, *29* (5), 347–364. https://doi.org/10.1038/s41422-019-0164-5.(27) Bertheloot, D.; Latz, E.; Franklin, B. S. Necroptosis, Pyroptosis and Apoptosis: An Intricate Game of Cell Death. *Cell. Mol. Immunol.* **2021**, *18* (5), 1106–1121.

(28) Parida, S.; Maiti, C.; Rajesh, Y.; Dey, K. K.; Pal, I.; Parekh, A.; Patra, R.; Dhara, D.; Dutta, P. K.; Mandal, M. Gold Nanorod Embedded Reduction Responsive Block Copolymer Micelle-Triggered Drug Delivery Combined with Photothermal Ablation for Targeted Cancer Therapy. *Biochim. Biophys. Acta - Gen. Subj.* **2017**, *1861* (1), 3039–3052.

(29) Sharifi, M.; Hosseinali, S. H.; Saboury, A. A.; Szegezdi, E.; Falahati, M. Involvement of Planned Cell Death of Necroptosis in Cancer Treatment by Nanomaterials: Recent Advances and Future Perspectives. *J. Control. Release* **2019**, *299*, 121–137.

(30) Nicosia, A.; Cavallaro, G.; Costa, S.; Utzeri, M.; Cuttitta, A.; Giammona, G.; Mauro, N. Carbon Nanodots for On Demand Chemophotothermal Therapy Combination to Elicit Necroptosis: Overcoming Apoptosis Resistance in Breast Cancer Cell Lines. *Cancers (Basel).* **2020**, *12* (11), 3114.

(31) Zhao, H.; Chen, H.; Guo, Z.; Zhang, W.; Yu, H.; Zhuang, Z.; Zhong, H.; Liu, Z. In Situ Photothermal Activation of Necroptosis Potentiates Black Phosphorus-Mediated Cancer Photo-Immunotherapy. *Chem. Eng. J.* **2020**, *394*, 124314.

(32) Chen, W.; Wang, X.; Zhao, B.; Zhang, R.; Xie, Z.; He, Y.; Chen, A.; Xie, X.; Yao, K.; Zhong, M.; Yuan, M. CuS–

MnS 2 Nano-Flowers for Magnetic Resonance Imaging Guided Photothermal/Photodynamic Therapy of Ovarian Cancer through Necroptosis. *Nanoscale* **2019**, *11* (27), 12983–12989.

(33) Liu, C.; Li, P.; Qu, Z.; Xiong, W.; Liu, A.; Zhang, S. Advances in the Antagonism of Epigallocatechin-3-Gallate in the Treatment of Digestive Tract Tumors. *Molecules* **2019**, *24* (9), 1726.

(34) Zhang, Y.; Zhan, X.; Xiong, J.; Peng, S.; Huang, W.; Joshi, R.; Cai, Y.; Liu, Y.; Li, R.; Yuan, K.; Zhou, N.; Min, W. Temperature-Dependent Cell Death Patterns Induced by Functionalized Gold Nanoparticle Photothermal Therapy in Melanoma Cells. *Sci. Rep.* **2018**, *8* (1), 8720.

(35) Shankar, S. Green Tea Polyphenols: Biology and Therapeutic Implications in Cancer. *Front. Biosci.* **2007**, *12* (12), 4881.

(36) Sanna, V.; Singh, C. K.; Jashari, R.; Adhami, V. M.; Chamcheu, J. C.; Rady, I.; Sechi, M.; Mukhtar, H.; Siddiqui, I. A. Targeted Nanoparticles Encapsulating (−)-Epigallocatechin-3-Gallate for Prostate Cancer Prevention and Therapy. *Sci. Rep.* **2017**, *7* (1), 41573.

(37) Shimizu, M.; Shirakami, Y.; Sakai, H.; Yasuda, Y.; Kubota, M.; Adachi, S.; Tsurumi, H.; Hara, Y.; Moriwaki, H. (−)-Epigallocatechin Gallate Inhibits Growth and Activation of the VEGF/VEGFR Axis in Human Colorectal Cancer Cells. *Chem. Biol. Interact.* **2010**, *185* (3), 247–252.

(38) Zhang, L.; Xie, J.; Gan, R.; Wu, Z.; Luo, H.; Chen, X.; Lu, Y.; Wu, L.; Zheng, D. Synergistic Inhibition of Lung Cancer Cells by EGCG and NF-KB Inhibitor BAY11-7082. *J. Cancer* **2019**, *10* (26), 6543–6556.

(39) Sharifi-Rad, M.; Pezzani, R.; Redaelli, M.; Zorzan, M.; Imran, M.; Ahmed Khalil, A.; Salehi, B.; Sharopov, F.; Cho, W. C.; Sharifi-Rad, J. Preclinical Activities of Epigallocatechin Gallate in Signaling Pathways in Cancer. *Molecules* **2020**, *25* (3), 467.

(40) Peng, Y.; Meng, Q.; Zhou, J.; Chen, B.; Xi, J.; Long, P.; Zhang, L.; Hou, R. Nanoemulsion Delivery System of Tea Polyphenols Enhanced the Bioavailability of Catechins in Rats. *Food Chem.* **2018**, *242*, 527–532.

(41) Li, K.; Teng, C.; Min, Q. Advanced Nanovehicles-Enabled Delivery Systems of Epigallocatechin Gallate for Cancer Therapy. *Front. Chem.* **2020**, *8*, 1-9.

(42) Ding, J.; Liang, T.; Min, Q.; Jiang, L.; Zhu, J.-J. "Stealth and Fully-Laden" Drug Carriers: Self-Assembled Nanogels Encapsulated with Epigallocatechin Gallate and SiRNA for Drug-Resistant Breast Cancer Therapy. *ACS Appl. Mater. Interfaces* **2018**, *10* (12), 9938–9948.

(43) Wang, W.; Chen, D.; Zhu, K. SOX2OT Variant 7 Contributes to the Synergistic Interaction between EGCG and Doxorubicin to Kill Osteosarcoma via Autophagy and Stemness Inhibition. *J. Exp. Clin. Cancer Res.* **2018**, *37* (1), 37.

(44) Mun, S. T.; Bae, D. H.; Ahn, W. S. Epigallocatechin Gallate with Photodynamic Therapy Enhances Anti-Tumor Effects in Vivo and in Vitro. *Photodiagnosis Photodyn. Ther.* **2014**, *11* (2), 141–147.

(45) Chen, X.; Yi, Z.; Chen, G.; Ma, X.; Su, W.; Cui, X.; Li, X. DOX-Assisted Functionalization of Green Tea Polyphenol Nanoparticles for Effective Chemo-Photothermal Cancer Therapy. *J. Mater. Chem. B* **2019**, *7* (25), 4066–4078.

(46) Li, S.; Lui, K.-H.; Tsoi, T.-H.; Lo, W.-S.; Li, X.; Hu, X.; Chi-Shing Tai, W.; Hiu-Ling Hung, C.; Gu, Y.-J.; Wong, W.-T. PH-Responsive Targeted Gold Nanoparticles for in Vivo Photoacoustic Imaging of Tumor Microenvironments. *Nanoscale Adv.* **2019**, *1* (2), 554–564.

(47) Liu, C.; Li, S.; Gu, Y.; Xiong, H.; Wong, W.; Sun, L. Multispectral Photoacoustic Imaging of Tumor Protease Activity with a Gold Nanocage-Based Activatable Probe. *Mol. Imaging Biol.* **2018**, *20* (6),

919–929.

(48)   Chen, J.; Saeki, F.; Wiley, B. J.; Cang, H.; Cobb, M. J.; Li, Z.-Y.; Au, L.; Zhang, H.; Kimmey, M. B.; Li, X.; Xia, Y. Gold Nanocages: Bioconjugation and Their Potential Use as Optical Imaging Contrast Agents. *Nano Lett.* **2005**, *5* (3), 473–477.

(49)   You, J.; Zhang, G.; Li, C. Exceptionally High Payload of Doxorubicin in Hollow Gold Nanospheres for Near-Infrared Light-Triggered Drug Release. *ACS Nano* **2010**, *4* (2), 1033–1041.

(50)   Li, W.; Brown, P. K.; Wang, L. V.; Xia, Y. Gold Nanocages as Contrast Agents for Photoacoustic Imaging. *Contrast Media Mol. Imaging* **2011**, *6* (5), 370–377.

(51)   Fang, X.; Lui, K.-H.; Li, S.; Lo, W.-S.; Li, X.; Gu, Y.; Wong, W. Multifunctional Nanotheranostic Gold Nanocage/Selenium Core-Shell for PAI-Guided Chemo-Photothermal Synergistic Therapy in Vivo. *Int. J. Nanomedicine* **2020**, *Volume 15*, 10271–10284.

(52)   Makadia, H. K.; Siegel, S. J. Poly Lactic-Co-Glycolic Acid (PLGA) as Biodegradable Controlled Drug Delivery Carrier. *Polymers (Basel).* **2011**, *3* (3), 1377–1397.

(53)   Musumeci, T.; Ventura, C. A.; Giannone, I.; Ruozi, B.; Montenegro, L.; Pignatello, R.; Puglisi, G. PLA/PLGA Nanoparticles for Sustained Release of Docetaxel. *Int. J. Pharm.* **2006**, *325* (1–2), 172–179.

(54)   Gu, J.-W.; Makey, K. L.; Tucker, K. B.; Chinchar, E.; Mao, X.; Pei, I.; Thomas, E. Y.; Miele, L. EGCG, a Major Green Tea Catechin Suppresses Breast Tumor Angiogenesis and Growth via Inhibiting the Activation of HIF-1α and NFκB, and VEGF Expression. *Vasc. Cell* **2013**, *5* (1), 9.

(55)   Tang, W.; Song, H.; Cai, W.; Shen, X. Real Time Monitoring of Inhibition of Adipogenesis and Angiogenesis by (−)-Epigallocatechin-3-Gallate in 3T3-L1 Adipocytes and Human Umbilical Vein Endothelial Cells. *Nutrients* **2015**, *7* (10), 8871–

8886.

(56)   Zhang, L.; Chen, W.; Tu, G.; Chen, X.; Lu, Y.; Wu, L.; and Zheng, D. Enhanced Chemotherapeutic Efficacy of PLGA-Encapsulated Epigallocatechin Gallate (EGCG) against Human Lung Cancer. *Int J Nanomedicine.* **2020**, *15*, 4417–4429.

(57)   Chuang, C.-C.; Cheng, C.-C.; Chen, P.-Y.; Lo, C.; Chen, Y.-N.; Shih, M.-H.; Chang, C.-W. Gold Nanorod-Encapsulated Biodegradable Polymeric Matrix for Combined Photothermal and Chemo-Cancer Therapy. *Int. J. Nanomedicine* **2018**, *Volume 14*, 181–193.

(58)   Li, S.; Lui, K.-H.; Li, X.; Fang, X.; Lo, W.-S.; Gu, Y.-J.; Wong, W.-T. PH-Triggered Poly(Ethylene Glycol)–Poly(Lactic Acid/Glycolic Acid)/Croconaine Nanoparticles-Assisted Multiplexed Photoacoustic Imaging and Enhanced Photothermal Cancer Therapy. *ACS Appl. Bio Mater.* **2021**, *4* (5), 4152–4164.

(59)   Laster, S.M.; Wood, J.G; Gooding, L.R. Tumor Necrosis Factor Can Induce Both Apoptic and Necrotic Forms of Cell Lysis. *J Immunol .* **1988**, *141* (8), 2629–2634.

(60)   Huang, Y.-J.; Wang, K.-L.; Chen, H.-Y.; Chiang, Y.-F.; Hsia, S.-M. Protective Effects of Epigallocatechin Gallate (EGCG) on Endometrial, Breast, and Ovarian Cancers. *Biomolecules* **2020**, *10* (11), 1481.

(61)   Zhang, Q.; Tang, X.; Lu, Q.; Zhang, Z.; Rao, J.; Le, A. D. Green Tea Extract and (−)-Epigallocatechin-3-Gallate Inhibit Hypoxia- and Serum-Induced HIF-1α Protein Accumulation and VEGF Expression in Human Cervical Carcinoma and Hepatoma Cells. *Mol. Cancer Ther.* **2006**, *5* (5), 1227–1238.

(62)   Schito, L.; Semenza, G. L. Hypoxia-Inducible Factors: Master Regulators of Cancer Progression. *Trends in Cancer* **2016**, *2* (12), 758–770.

(63)   Wu, Y.; Dong, G.; Sheng, C. Targeting Necroptosis in Anticancer Therapy: Mechanisms and Modulators. *Acta Pharm. Sin. B* **2020**, *10* (9), 1601–1618.